PHYSICSAccess Research Paper
ISSN Online: 2756-3898, ISSN Print: 2714-500X https://doi.org/10.47514/phyaccess.2026.6.2.009

First-principles Investigation of Structural, Electronic, Mechanical, Optical, and Thermodynamic Properties of Lead-Free $KSrX_3$ (X = F, Cl, and Br) Halide Perovskites for UV Optoelectronic Applications

Rose P Abang[1], Auwalu Musa[1], Reuben A Solomon[1], Abdulkadir S Gidado[1], and Sylvester Hassan[2]

[1] Department of Physics, Bayero University Kano, Kano State, Nigeria
[2] Department of Physics, Federal University Gashua, Yobe State, Nigeria

Corresponding E-mail: solomonreuben1010@gmail.com

Received 23-05-2026
Accepted for publication 07-07-2026
Published 22-07-2026

Abstract

This study employed density functional theory (DFT) within Quantum ESPRESSO to investigate the structural, electronic, phonon, mechanical, optical, and thermodynamic properties of cubic $KSrX_3$ (X = F, Cl, Br) halide perovskites for UV optoelectronic applications. All compounds were found to be structurally, thermodynamically, mechanically, and dynamically stable, as confirmed by negative formation energies, appropriate Goldschmidt tolerance factors, Born stability criteria, and phonon spectra without imaginary frequencies. $KSrF_3$ exhibited a direct band gap of 5.52 eV, while $KSrCl_3$ and $KSrBr_3$ showed indirect band gaps of 4.45 and 3.75 eV, respectively, making $KSrF_3$ the most promising candidate for deep-UV applications. The compounds exhibited ductile behavior, characterized by dominant ionic bonding, low Debye temperatures indicative of low lattice thermal conductivity, and thermodynamic properties consistent with the third law of thermodynamics and Dulong–Petit's law. Optical calculations revealed strong UV absorption and static dielectric constants of 2.02, 2.46, and 2.56 for $KSrF_3$, $KSrCl_3$, and $KSrBr_3$, respectively, highlighting their potential for UV optoelectronic devices.

Keywords: DFT; Halides Perovskites; Thermodynamic Properties; Optical properties; Elastic and Optoelectronic properties.

I. Introduction

The global challenge of the growing energy crisis, the fast depletion of fossil fuels, and associated environmental risks such as global warming affect the growth of every nation's economy [1-2]. The quest for environmentally friendly renewable energy technologies has led to research in various materials suitable for photovoltaic applications. Halide perovskites have recently emerged as a class of potential photovoltaic and optoelectronic materials [3-4].

A perovskite is a crystal generally having the formula ABX_3, consisting of A: a large monovalent cation (e.g., K^+, Cs^+ or organic ions like methylammonium, MA), which

occupies the spaces of a octahedron; B: a smaller divalent metal cation (e.g., Pb^{2+}, Sn^{2+}, Sr^{2+}) which sits at the centre of an octahedron formed by X atoms, and X: a monovalent anion, often oxygen (O^{2-}) or a halide (F^-, Cl^-, Br^-, I^-) [5-6]. Recent research, such as the incorporation of halide perovskite materials as light absorbers, has greatly increased the power conversion efficiency of photovoltaic (PV) solar cells from around 3.8% in 2009 to about 25% in 2019 [7-8].

Perovskite materials have gained prominent attention in PV technology because of their phenomenal properties in aspects of high thermoelectric power, charge ordering, spin-dependent transport, and vast interactions between structural, magnetic, electronic, and optical characteristics [9]. The wide range of these potential applications of halide perovskite in PV cells, optoelectronics, LEDs, laser device and photodetectors stems from excellent optoelectronic properties such as bandgap tunability [10], compositional flexibility, where a wide range of elemental substitution at the A, B, and X sites is possible [11], and a relatively cheap production method [12], as well as an inexpensive computational cost.

Artificial Neural Networks (ANN) have been employed to predict the properties of several halide perovskites, including $XSrBr_3$ (X = Li, K, Ag) [13]. These compounds exhibit wide band gaps of 6.31, 6.59, and 4.17 eV, respectively, together with promising optical properties, making them attractive candidates for ultraviolet (UV) photodetectors, deep-UV light-emitting diodes (LEDs), and high-frequency electronic applications [14]. The A-site cation plays a crucial role in maintaining the structural stability of the perovskite lattice [14]. Previous investigations of $KSrX_3$ (X = F and Cl) using the PBE-GGA, LDA, and WC exchange-correlation functionals have reported the structural, elastic, and optical properties of these compounds, revealing direct and indirect band gaps for the fluoride and chloride perovskites, respectively [15]. However, comprehensive investigations of the $KSrX_3$ (X = F, Cl, Br) family remain limited, particularly with respect to phonon, thermodynamic, and mechanical properties. This lack of information hinders a complete understanding of their stability and potential for UV optoelectronic applications.

The present study employs first-principles density functional theory (DFT) calculations, as implemented in Quantum ESPRESSO, to systematically investigate the structural, electronic, phonon, mechanical, optical, and thermodynamic properties of cubic $KSrX_3$ (X = F, Cl, Br). Emphasis is placed on elucidating the influence of halide substitution on structural stability, thermodynamic behavior, and UV optoelectronic response, to assess the suitability of these lead-free perovskites for high-frequency UV optoelectronic applications.

II. Computational Method

First principles calculations of $KSrX_3$ (X = F, Cl, and Br) were carried out using the Quantum ESPRESSO software package [16]. Projected augmented-wave (PAW) pseudopotentials were used to describe the electron-to-ion interactions. The exchange-correlation effects included the GGA-PBE functionals [17]. To minimize errors, a self-consistent convergence was achieved for all calculations. The optimized plane wave cutoff was obtained at 40 Ry, while the Morkhorst-Pack K-point sampling scheme of the Brillouin zone (BZ) was achieved at a level of 10 x 10 x 10 k-point were utilized. Optimized crystal structures were analyzed and viewed using XCrysden and VESTA software. The optimized crystal parameters were then employed to construct the Morgan equation of states (EOS) to compute Mechanical and thermodynamic properties using Thermo_pw. All self-consistent field calculations were performed using an energy convergence threshold of 10^{-5} Ry [18]. Optical properties were calculated by solving the Kramers-Kronig relations [19]. The plane wave energy cut-off and convergence are shown in Fig. 1(a) and (b).

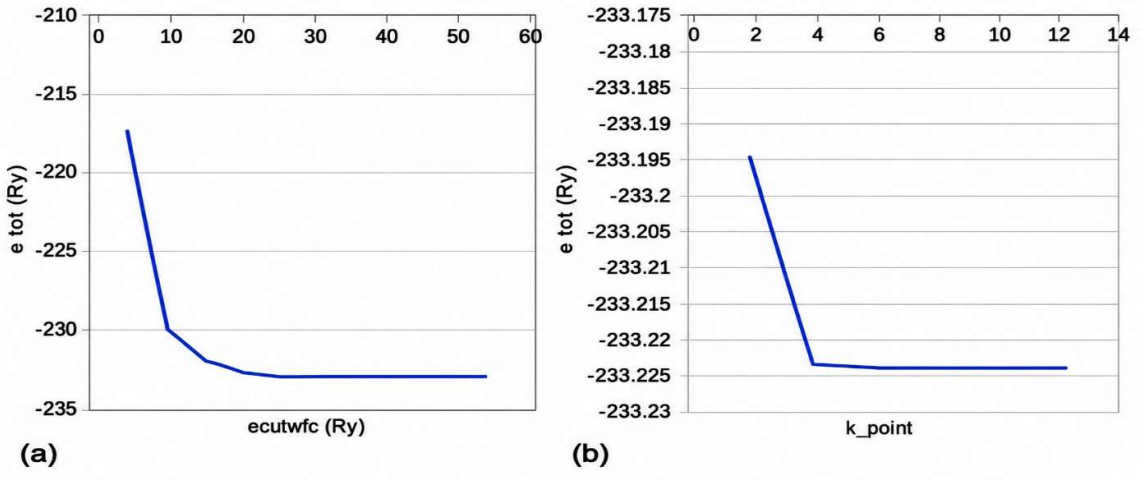

Fig. 1. (a) Wave function (b) K-points optimization for $KSrCl_3$.

III. Results and Discussion

A. Structural Properties

Fig. 2 depicts the $KSrX_3$ (X = F, Cl, Br) compounds crystallize in the ideal cubic perovskite structure with space group *Pm*3*m* (No. 221, point group).

In this arrangement, the K cation occupies the A site at the corner positions (0, 0, 0), the Sr cation occupies the B-site at the body-centre (½, ½, ½), while the X atoms occupy the face-centered positions at (0, ½, ½). The optimized structural parameters, including the lattice constant *a*, unit cell volume V_0, ground state energy E_{min}, formation energy, E_f, interatomic bond lengths, Goldschmidt tolerance factor *t*, and carrier effective masses, are listed in Table I. Tolerance factor and formation energy help in gaining knowledge on materials' structural and thermodynamic stability [4], [20].

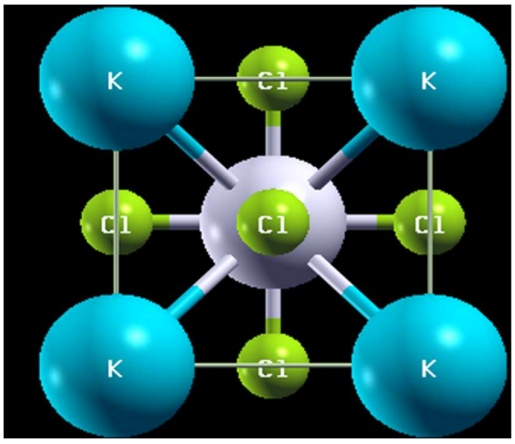

Fig. 2.. Optimized crystal structure of $KSrCl_3$.

Table I. Calculated structural parameters of $KSrX_3$ (X = F, Cl, Br): space group, lattice constant *a*, unit cell volume V_0, ground state energy E_{min}, formation energy E_f, interatomic bond lengths, Goldschmidt tolerance factor *t*, and carrier effective masses m_e and m_h.

Parameter	$KSrF_3$	$KSrCl_3$	$KSrBr_3$
Space group	Pm3m (No. 221)	Pm3m (No. 221)	Pm3m (No. 221)
Lattice constant a (Å)	4.7647	5.6837	5.9854
Unit cell volume V_0 (Å³)	108.17	183.61	214.43
Ground state energy E_{min} (Ry)	−275.848	−233.596	−219.141
Formation energy E_f (eV/atom)	−3.430	−2.308	−2.106
d_{K-X} bond length (Å)	3.3692	4.0190	4.2323
d_{Sr-X} bond length (Å)	2.3824	2.8418	2.9928
Tolerance factor t	0.99984	0.99984	0.99984
Electron eff. mass $m_{e\,(m_0)}$	0.340	0.4294	0.420
Hole eff. mass $m_{h\,(m_0)}$	0.496	0.023	0.9324

The equilibrium volume V_o, bulk modulus B_0 was obtained by fitting total energy (E) against calculated volume, V (see Fig 3), into the Morgan equation of states (EOS) as given in (1) [21];

$$E(V) = \frac{B_0}{B_o'}\left[\left(\left(\frac{V_o}{V}\right)^{B_o'}\right)\frac{1}{B_o'} + 1\right] + Constant \qquad (1)$$

The equilibrium lattice constants, derived from the optimized unit cell volumes as $a = {V_o}^{1/3}$, are 4.7647 Å, 5.6837 Å, and 5.9854 Å for $KSrF_3$, $KSrCl_3$, and $KSrBr_3$, respectively (see Fig. 3). The lattice constant values agree with prior research data [14-15], [22]. These values increase monotonically with the halide ionic radius, following the expected trend $F^- < Cl^- < Br^-$, since the enlargement of the anion pushes the A- and B-site cations apart, expanding the unit cell. The corresponding unit cell volumes are 108.17 Å³, 183.61 Å³, and 214.43 Å³, reflecting the same trend of lattice expansion from fluoride to bromide.

The thermodynamic stability of the three compounds was evaluated through the formation energy per atom E_f using (2) [23].

$$E_f = \frac{1}{N}\left[E_{KSrX_3} - (E_K + E_{Sr} + 3E_X)\right] \qquad (2)$$

where E_f, is the formation energy in eV/atom, E_{KSrX_3} the total energy of the perovskite, E_K, E_{Sr} and E_X are the energy (in eV) of K, Sr, and X, respectively, and N is the total number of atoms in the system.

The computed values are −3.430 eV/atom ($KSrF_3$), −2.308 eV/atom ($KSrCl_3$), and −2.106 eV/atom ($KSrBr_3$). The values are close to -1.12 eV/atom [14] and -3.410 eV/atom [22] obtained in previous research. All three formation energies are negative, confirming that the compounds are thermodynamically stable [20]. The most negative value for $KSrF_3$ indicates that it is the most thermodynamically stable member of the series.

The structural stability of the perovskite phase was further assessed using the derived bond length form of the empirical Goldschmidt tolerance factor, defined as in (3) [24].

$$t = \frac{0.707(d_{K-X})}{d_{Sr-X}} \qquad (3)$$

where d_{K-X} is the bond length between K and X, and d_{Sr-X} between Sr and X, respectively. Equation (3) is adopted over the classical ionic radius expression because radii are formal constructs that can vary with coordination, oxidation state, spin state, and degree of covalency, whereas DFT

relaxed bond lengths provide a direct, structure-specific measure of the local atomic environment. The computed tolerance factor is $t \sim 0.9998$ for all three compounds (see Table I), a value remarkably close to unity. According to the Goldschmidt stability criterion, an ideal cubic perovskite corresponds to $t = 1$, and stable perovskite formation is generally expected for $0.80 \leq t \leq 1.05$ [25]. The near-unity values obtained confirm that $KSrF_3$, $KSrCl_3$, and $KSrBr_3$ all adopt and maintain the ideal cubic perovskite phase with negligible structural distortion.

The interatomic bond lengths (See Table I) provide further insight into the structural chemistry of the series. Both K–X and Sr–X distances increase progressively with halide size, as expected from the increase in the lattice constant. The Sr–X bond is consistently shorter than the K–X bond, which reflects the higher charge (+2) and smaller coordination number of the B-site Sr^{2+} relative to the twelve-coordinated A-site K^+ ion.

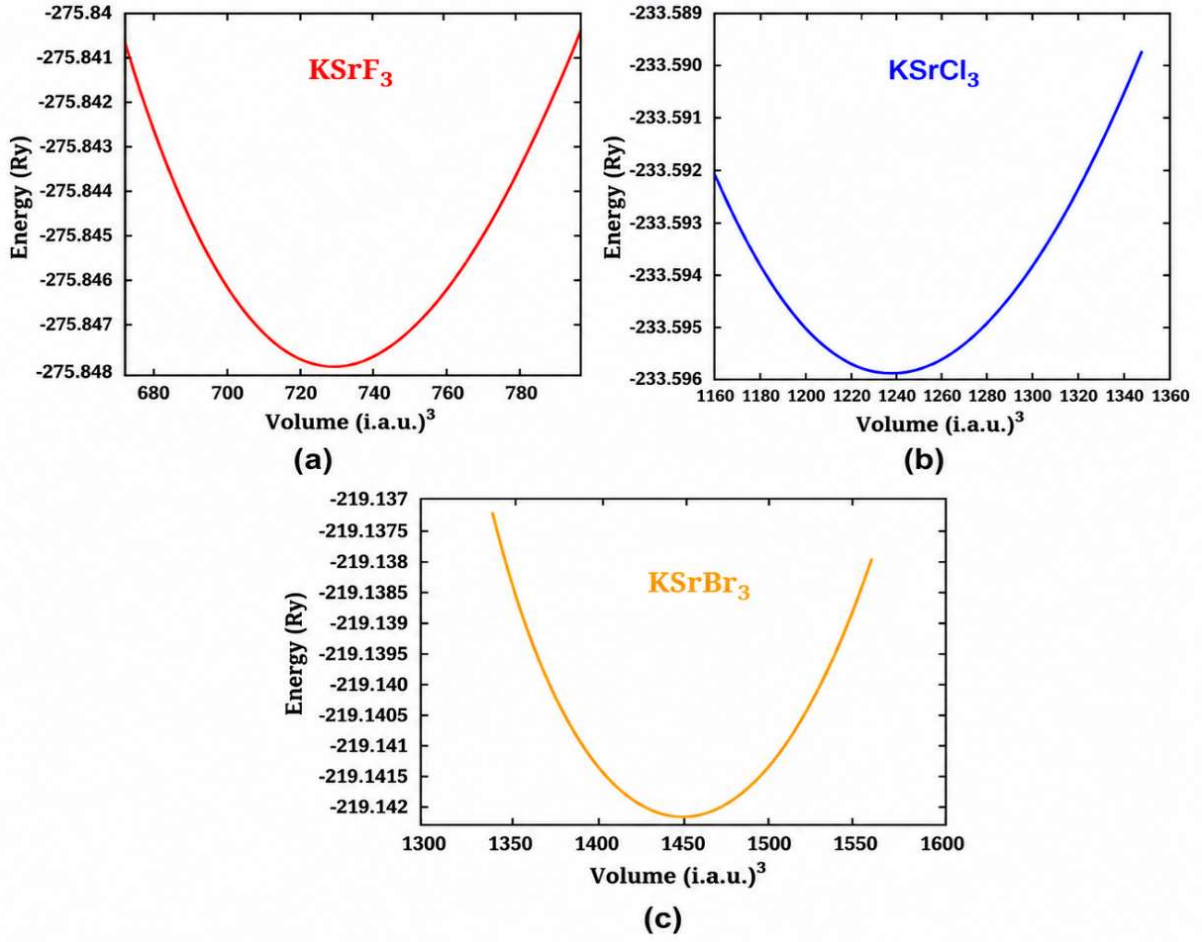

Fig. 3. Fitted energy-volume curve of compounds (a) $KSrF_3$ (b) $KSrCl_3$ (c) $KSrBr_3$

B. Electronic properties

1) Band Structure

The electronic structures of the $KSrX_3$ (X = F, Cl, Br) halide perovskite series were investigated through their band structures with the Fermi energy set to zero in all cases, as shown in Fig. 4 (see next page). $KSrF_3$ exhibits a direct band gap of 5.52 eV at the Γ high-symmetry point, where both the valence band maximum (VBM) and conduction band minimum (CBM) are located at the same k-point. $KSrCl_3$ and $KSrBr_3$, by contrast, display indirect band gaps of 4.45 eV and 3.75 eV, respectively, with the VBM situated at the R (or M) point and the CBM at the Γ point in both compounds. The band gap obtained in this study is consistent with the computation results [3], [15], [22], for the same functionals, confirming the reliability of our calculation. Comparing the band gap value from this work for KSrBr3, with a value of 6.19 eV reported by [14], using the TB-mBJ potential further confirms the well-known tendency of GGA-PBE to underestimate band gaps.

The progressive reduction in band gap from F to Cl to Br reflects the decreasing electronegativity and increasing polarizability of the halide anion, a trend commonly observed

across halide perovskite families. All three compounds fall within the wide band gap semiconductor regime (Eg > 3 eV), making them electrically insulating under ambient conditions and optically transparent across much of the visible spectrum. Such wide gaps render them promising candidates for deep-ultraviolet (DUV) optoelectronics applications, with $KSrF_3$, owing to its largest gap, being most suitable for DUV or vacuum-UV devices.

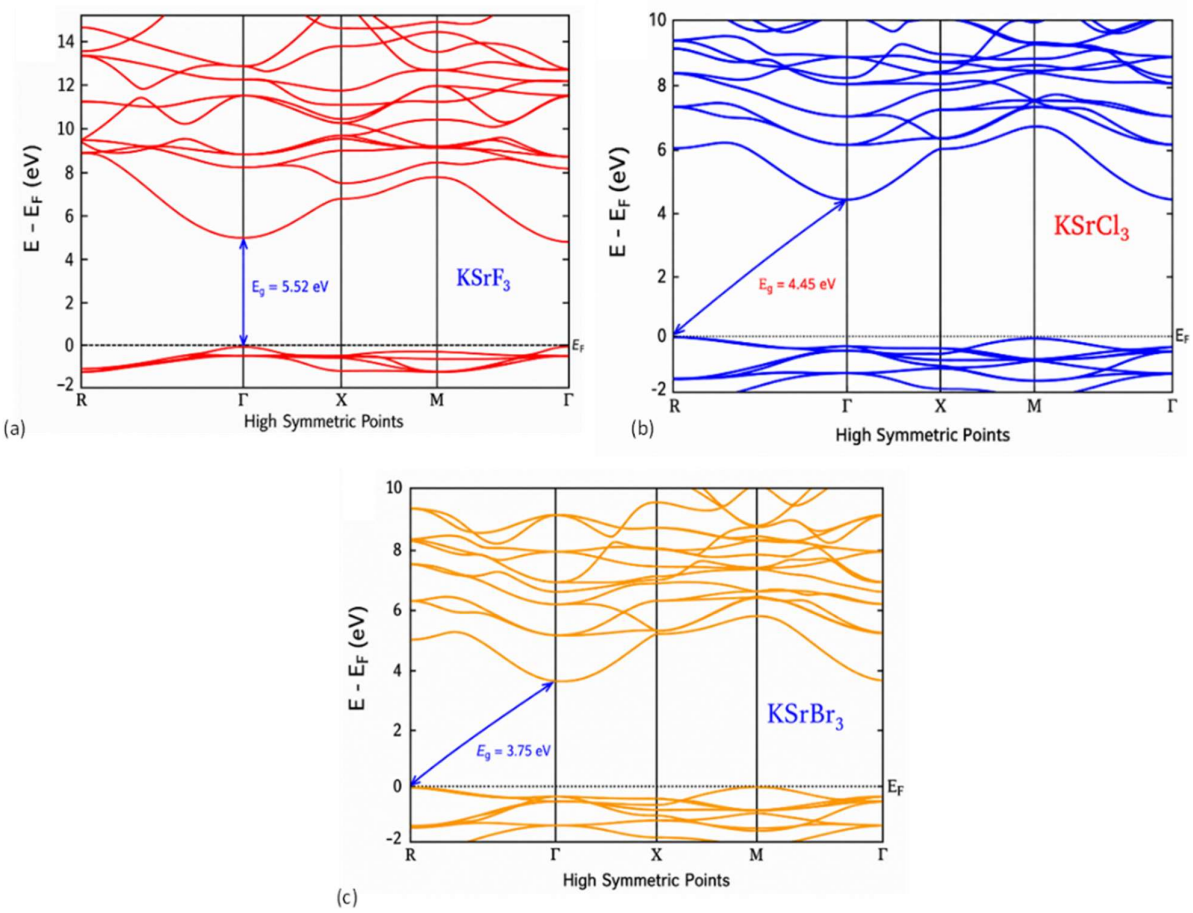

Fig. 4. The electronic band structure of compounds (a) $KSrF_3$, (b) $KSrCl_3$, and (c) $KSrBr_3$.

2) Density of states (DOS)

Analysis of the total and partial DOS in Fig. 5 (see next page) reveals that the halide p-states overwhelmingly dominate the valence band region immediately below the Fermi level in all three compounds. In $KSrF_3$, the F p-orbitals account for virtually the entire VBM contribution, with negligible Sr-d and K-p character, indicating a highly ionic and electronically localized valence band. In $KSrCl_3$ and $KSrBr_3$, the Cl and Br states similarly govern the upper valence band, respectively, though with slightly broader band widths consistent with the greater spatial extent of the heavier halide orbitals.

The conduction band, conversely, is primarily composed of Sr and K states, with Sr orbital character becoming increasingly evident toward the CBM, suggesting that photoexcited electrons would reside predominantly on the Sr sublattice. The deep valence features observed around −12 to −15 eV (F), −13 to −15 eV (Cl), and −12 to −13 eV (Br) correspond to lower-lying halide states hybridized with cation contributions.

2) Effective Mass

The carrier effective masses m_e and m_h calculated using curve fitting are included in Table I as they reflect the curvature of the electronic band structure at the VBM and CBM and govern the charge transport properties of the material. To the best of our knowledge, no prior study has reported the effective masses of carriers for $KSrF_3$, $KSrCl_3$, and $KSrBr_3$; the values presented here therefore constitute the first theoretical predictions for these compounds. In the absence of direct literature counterparts, we compare our effective masses with those of isostructural halide perovskites sharing the same A-site (K^+) cation, particularly $KGeCl_3$ [26], which provides a meaningful structural and chemical analogy.

The electron effective mass m_e ranges from $0.340m_0$ ($KSrF_3$) to $0.4294m_0$ ($KSrCl_3$) and $0.420m_0$ ($KSrBr_3$), which

are acceptable in comparison to the value obtained for cubic $KGeCl_3$ and $RbGeCl_3$ by [1], [26]. These moderate values affect masses and reflect a reasonably dispersive conduction band minimum, which is favorable for electron transport. In contrast, the hole effective mass m_h exhibits a strikingly non-monotonic variation: $0.496m_o$ in $KSrF_3$, dropping sharply to $0.023m_0$ in $KSrCl_3$, and rising to $0.932m_o$ in $KSrBr_3$. The exceptionally small hole effective mass in $KSrCl_3$ ($0.023m_0$) is particularly remarkable. Such a light hole mass is uncommon among halide perovskites and suggests a highly dispersive valence band maximum (VBM), which may originate from strong hybridization between the Cl-3p and Sr-4d or K-3p orbitals at the VBM. In contrast, the large m_h of $0.9324m_0$ in $KSrBr_3$ indicates a flat, localized VBM with suppressed hole transport, which may limit its performance in hole-transport-dependent applications such as solar cells but could be advantageous in electron-dominated photoconductors.

From a device perspective, the effective mass values have important implications. The small m_e across all three compounds suggests that electrons are the dominant mobile carriers, making the $KSrX_3$ series intrinsically n-type in character, consistent with the wide-bandgap halide perovskite family.

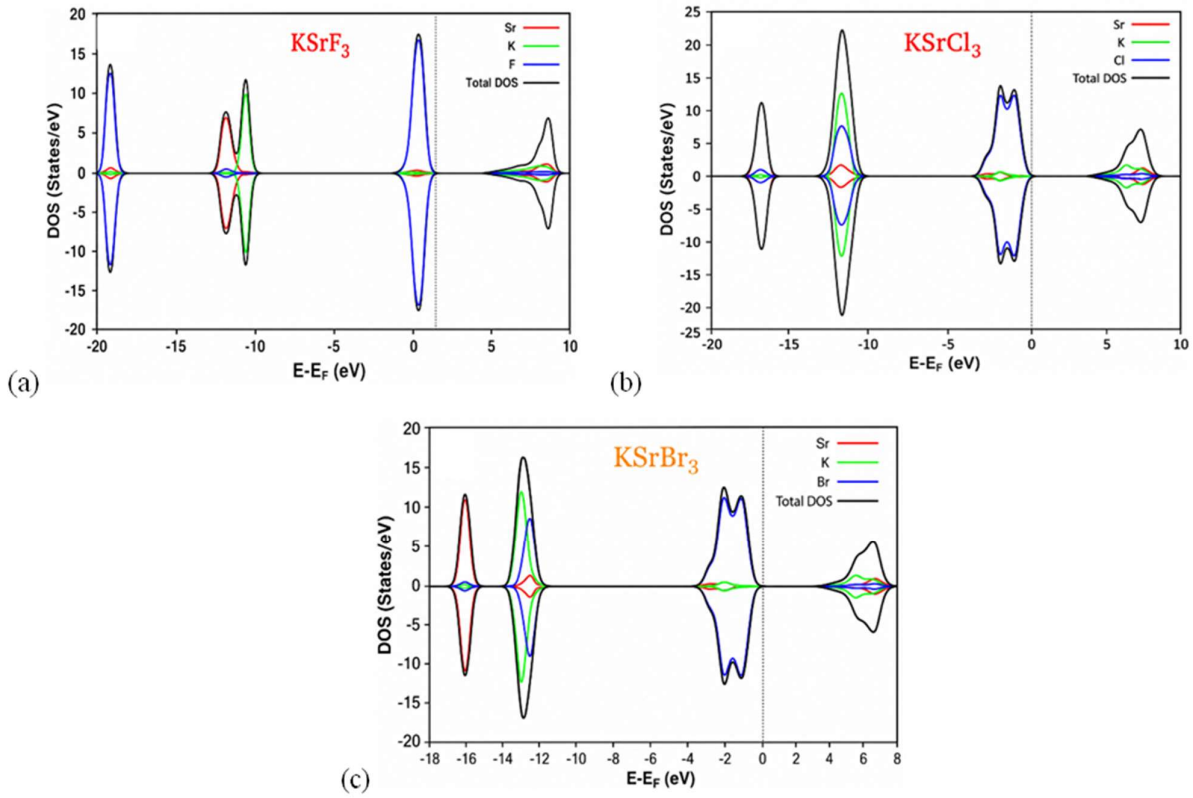

Fig. 5. PDOS of compounds (a) $KSrF_3$ (b) $KSrCl_3$ (c) $KSrBr_3$

3) Phonon Response

To further assess the stability of $KSrX_3$ (X = F, Cl, and Br) structures, we performed phonon dispersion calculations. The phonon band structures along the high symmetry k-path (Γ-X-M-Γ-R-X) in the BZ show no imaginary frequencies, as depicted by Fig. 6(a-c) (see next page). The absence of negative frequencies in the phonon dispersion curves of $KSrX_3$ suggests dynamical stability, consistent with findings for $XSrBr_3$ (X = Li, K, Ag) [14]. The high-frequency modes observed in $KSrX_3$ and the nature of their band gap indicate their potential for UV high-frequency device applications.

C. *Mechanical and Thermal Properties*

To investigate the mechanical behavior of $KSrX_3$ (X = F, Cl, Br), the three independent elastic constants C_{11}, C_{12}, and C_{44} characteristic of cubic crystal symmetry were computed via Thermo_pw within Quantum ESPRESSO. The mechanical stability of a cubic crystal is governed by the Born stability criteria, which require $C_{11} >$, $C_{44} > 0$, $C_{11} - C_{12} > 0$ $C_{11} + 2C_{12} > 0$ [21].

The elastic constants and Born stability values are listed in Table II. For $KSrX_3$. All Born stability conditions are satisfied for every compound, confirming their mechanical stability.

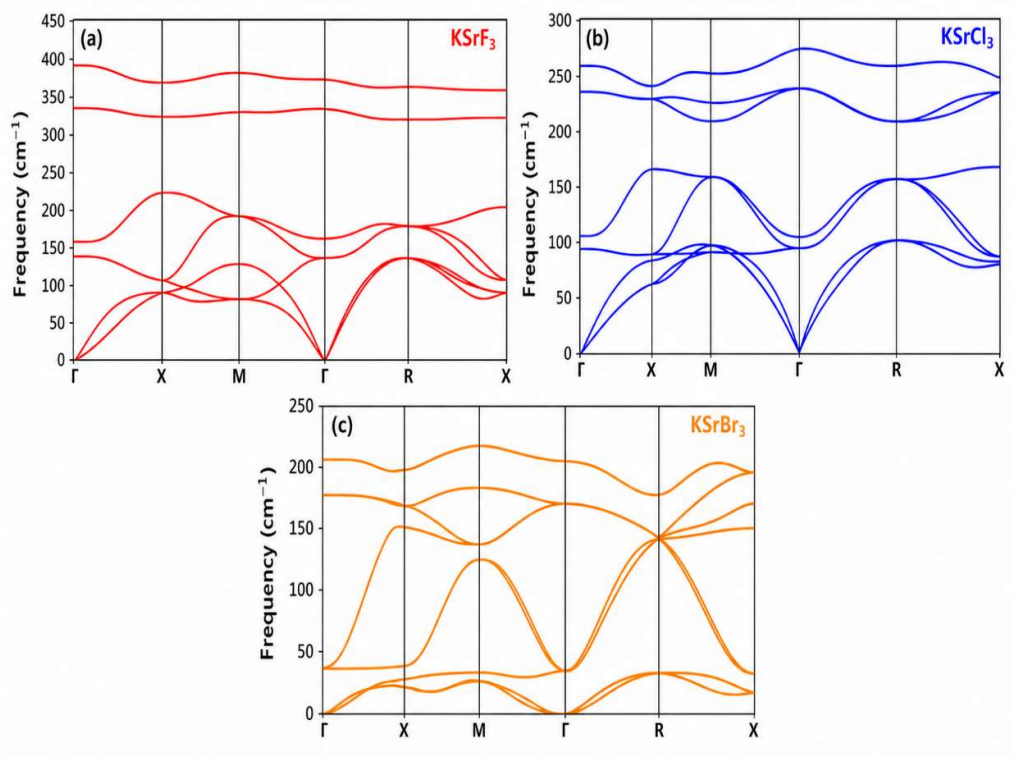

Fig. 6. Phonon dispersion curves for (a) $KSrF_3$, (b) $KSrCl_3$, and (c) $KSrBr_3$.

The progressive decrease in C_{11} from F to Br reflects lattice softening as the halide ionic radius increases, while the consistent dominance of C_{11} over C_{12} indicates stiffer resistance to unidirectional compression than to lateral strain.

Table II. Calculated elastic constants C_{11}, C_{12}, C_{44} (GPa), mass density ρ (g/cm³), VRH bulk modulus B, Young's modulus E, shear modulus G (GPa), and Poisson's ratio ν for $KSrX_3$ (X = F, Cl, Br).

Parameter	$KSrF_3$	$KSrCl_3$	$KSrBr_3$
$C_{11}\ (GPa)$	89.250	48.210	40.017
$C_{12}\ (GPa)$	13.480	6.046	4.661
$C_{44}\ (GPa)$	10.130	4.562	3.680
$C_{11} + 2C_{12}\ (GPa)$	116.210	60.302	49.339
$C_{11} - C_{12}\ (GPa)$	75.770	42.164	35.356
$\rho(g/cm^3)$	2.8052	2.0849	2.8382
$B(GPa)$	38.740	20.103	16.446
$G(GPa)$	17.780	8.909	7.332
$E(GPa)$	46.060	23.118	18.999
$\vartheta\ (Possion's\ ratio)$	0.29531	0.29747	0.29554

Using the Voigt–Reuss–Hill (VRH) averaging scheme [27-28], the bulk modulus B, shear modulus G, and Young's modulus E were obtained as presented in Table I. The bulk modulus, which measures resistance to volumetric compression, decreases from B = 38.74 GPa ($KSrF_3$) to 20.103 GPa ($KSrCl_3$) and 16.446 GPa ($KSrBr_3$), reflecting the increasingly compressible nature of the lattice with heavier halide substitution. The Young's modulus E similarly declines from 46.06 GPa to 23.118 GPa and 18.999 GPa, confirming that $KSrF_3$ is the stiffest compound and $KSrBr_3$ the most compliant in the series.

The ductile or brittle character of the $KSrX_3$ compounds is assessed through Pugh's ratio B/G and Poisson's ratio ν, as given in Table III. According to Pugh's criterion, a material is ductile when $B/G > 1.75$ and brittle otherwise [29]. The computed values of 2.179, 2.257, and 2.243 for $KSrF_3$, $KSrCl_3$, and $KSrBr_3$, respectively, all exceed this threshold, establishing ductile behaviour across the entire series. This is corroborated by the Frantsevich criterion [30], which classifies a material as ductile when ν > 0.26; the computed Poisson's ratios of 0.295, 0.297, and 0.296 are all consistently above this limit. The Cauchy pressure $C_{12} - C_{44}$ provides further insight into bonding character: positive values indicate dominant ionic bonding and ductility, while negative values suggest covalent character and brittleness. The values +3.350, +1.484, and +0.981 GPa for $KSrF_3$, $KSrCl_3$, and $KSrBr_3$ are all positive, confirming the ionic nature of the bonding and corroborating the ductile classification. The gradual decrease in Cauchy pressure along F → Cl → Br suggests a modest increase in covalent character as halide polarisability grows.

The elastic anisotropy is quantified by the Zener anisotropy index $A = 2C_{44}/(C_{11} - C_{12})$, where $A = 1$ corresponds to a perfectly isotropic material [31]. The computed values of 0.267, 0.216, and 0.208 deviate substantially from unity, confirming that all three compounds are elastically

anisotropic, with the degree of anisotropy increasing slightly from $KSrF_3$ to $KSrBr_3$. The machinability index $\mu_m = B/C_{44}$, which reflects the ease of plastic deformation during machining operations, increases progressively from 3.824 ($KSrF_3$) to 4.406 ($KSrCl_3$) and 4.469 ($KSrBr_3$), suggesting improved machinability in the chloride and bromide compounds.

Table III. Derived mechanical parameters: Pugh's ratio B/G, Cauchy pressure (GPa), Zener anisotropy index A, machinability index μ_m, acoustic wave velocities (m/s), Debye temperature, $\theta_D(K)$, and ductility classification for $KSrX_3$ (X = F, Cl, Br).

Parameter	$KSrF_3$	$KSrCl_3$	$KSrBr_3$
Cauchy pressure $C_{12} - C_{44}$ (GPa)	3.350	1.484	0.981
Zener anisotropy A	0.267	0.216	0.208
Machinability index $\mu_m = B/C_{44}$	3.824	4.406	4.469
$V_p(m/s)$	4705.566	3895.127	3039.919
$V_B(m/s)$	3706.207	3088.183	2407.440
$V_G(m/s)$	2510.933	2055.810	1607.494
$\theta_D(K)$	299.004	205.056	152.175
Pugh's ratio B/G	2.179	2.257	2.243
Ductile/Brittle	Ductile	Ductile	Ductile

The longitudinal (V_P), bulk (V_B), and shear (V_G) acoustic wave velocities all decrease monotonically across the series (Table III), consistent with the reduction in elastic moduli. The Debye temperature θ_D, which correlates with the dominant phonon frequency and thermal conductivity, follows the same trend: 299.004 K ($KSrF_3$) > 205.056 K ($KSrCl_3$) > 152.175 K ($KSrBr_3$). The highest θ_D for $KSrF_3$ reflects its stiffer interatomic bonding, while the lowest value for $KSrBr_3$ is consistent with its softer and more compliant lattice. The relatively low Debye temperatures across the series suggest low lattice thermal conductivity, which may be advantageous for thermoelectric applications.

D. Optical Properties

The optical response of a crystalline solid depends on the material's interaction with electromagnetic radiation and thereby determines its efficiency in applications like photonic, optoelectronic, and energy-harvesting technologies. For the $KSrX_3$ (X = F, Cl, Br) family of halide perovskites, the frequency-dependent complex dielectric function $\varepsilon(\omega) = \varepsilon_1(\omega) + i\varepsilon_2(\omega)$ was computed within the independent-particle approximation. All other linear optical quantities, such as refractive index n(ω), extinction coefficient K(ω), and absorption coefficient α(ω), are derived through the standard Kramers–Kronig consistent relations [19]. These parameters are paramount in assessing the efficiency of nano-electronics and optoelectronic devices [32]. The optical properties are depicted in Fig. 7.

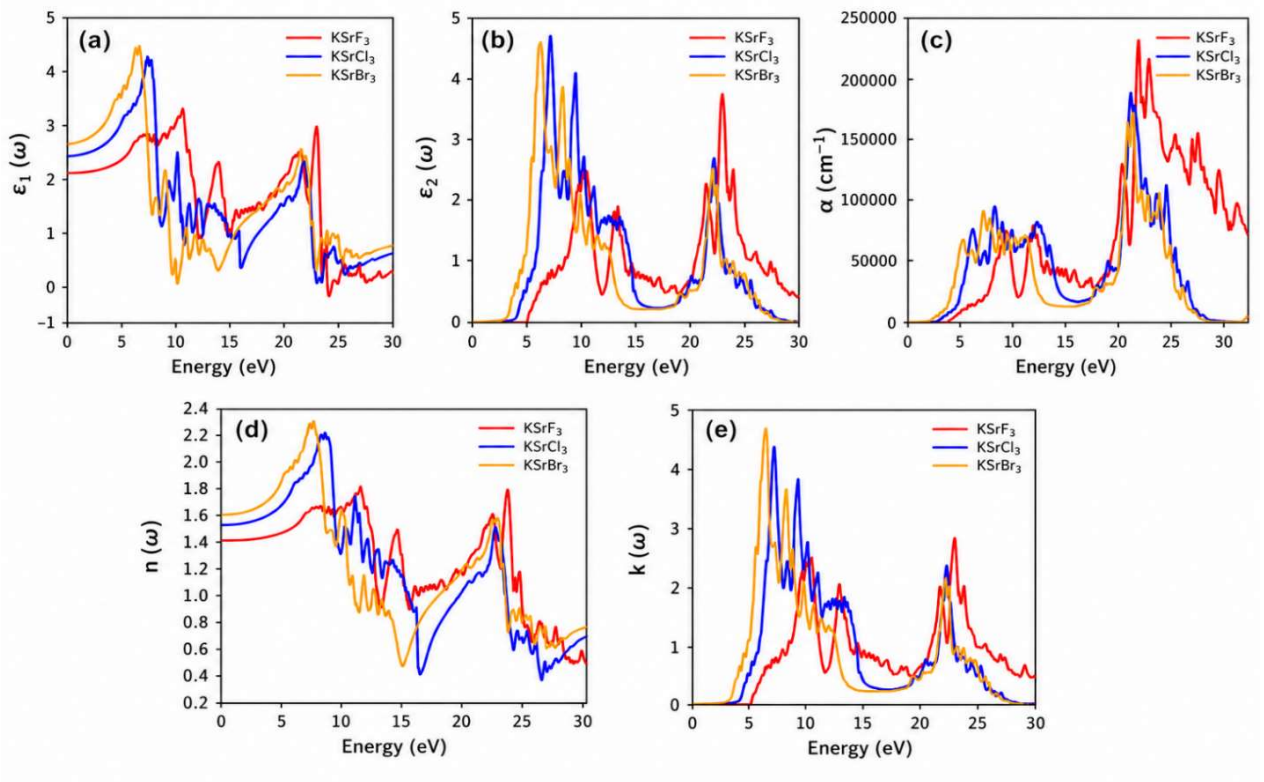

Fig. 7. Optical properties (a) Real and (b) Imaginary parts of complex dielectric function; (c) Absorption coefficient; (d) Refractive index, and (e) Extinction coefficient.

The real part of the dielectric function, $\varepsilon_1(\omega)$, as shown by Fig 7(a), reflects the polarization response of the lattice to an applied electric field. The static (zero-frequency) values $\varepsilon_1(0)$ extracted from the calculated spectra follow the sequence $KSrBr_3$ (≈ 2.54) > $KSrCl_3$ (≈ 2.46) > $KSrF_3$ (≈ 2.02), consistent with Mousa *et al*., [15]. This ordering is entirely consistent with the Penn model, which predicts an inverse dependence of $\varepsilon_1(0)$ on the optical band gap: as the halide anion is varied from F to Cl to Br, the gap narrows and the static dielectric constant increases accordingly. This can be due to the relatively low degree of bonding interaction found in the K and X ions in the larger halogen compounds. The decrease in peak height occurs because electronic transitions become less probable as the halogen ion gets larger.

Fig. 7(b) depicts the complex dielectric function of the $KSrF_3$ compounds $\varepsilon_2(\omega)$ to the photon energy. The onset energies are in close agreement with the corrected gaps quoted above, confirming the internal consistency of the calculation.

$KSrBr_3$ exhibits the lowest-energy onset near 3.75 eV and builds rapidly to a dominant first peak at approximately 4.8 eV with a peak height ≈ 4.75. This peak reflects strong optical coupling between Br valence states and the conduction band minimum, which carries appreciable Sr d character. $KSrCl_3$ follows with its onset near 4.45 eV; its main peak at approximately 5.5–6.0 eV reaches a height close to 4.1, again arising predominantly from Cl → Sr transitions. $KSrF_3$, which has the widest gap at 5.52 eV, shows a more gradual onset and a first peak near 8–9 eV of moderate intensity of ≈ 2.5. The significantly reduced oscillator strength in $KSrF_3$ at these energies reflects the deeper binding and smaller spatial extent of the F states compared with Cl and Br.

A secondary group of transitions centred near 20–22 eV is clearly resolved in all three spectra, appearing with comparable intensity across the series. Based on the partial density of states analysis, these features are assigned to optical excitations from the K and Sr semi-core levels, whose binding energies place them in precisely this energy window. The near-coincidence of this secondary structure across $KSrF_3$, $KSrCl_3$, and $KSrBr_3$ underscores its origin in the A-site and B-site cations rather than in the halide sublattice.

The refractive index $n(\omega) = \mathrm{Re}[\sqrt{\varepsilon(\omega)}]$ governs the phase velocity of light within the medium and determines the reflectance at normal incidence through the Fresnel coefficient. The static refractive indices n(0) are approximately 1.42, 1.57, and 1.59 for $KSrF_3$, $KSrCl_3$, and $KSrBr_3$, respectively. These are physically consistent with the $\varepsilon_1(0)$ values via the relation $n(0) = \sqrt{\varepsilon_1(0)}$ and follow the same trend with halide electronegativity: the more polarizable bromide anion yields the highest static index.

In the transparent region below the absorption edge, $n(\omega)$ increases slowly before rising steeply as the first absorption band is approached; a behavior characteristic of anomalous dispersion. The peak values of $n(\omega)$ are reached near the first prominent $\varepsilon_2(\omega)$ maximum, attaining approximately 2.28 for $KSrBr_3$ near 5.5 eV, 2.19 for $KSrCl_3$ near 6.5 eV, and about 1.79 for $KSrF_3$ near 8.5 eV. Beyond the peak, $n(\omega)$ falls rapidly through a broad minimum and remains depressed throughout the core absorption region (8–18 eV), recovering toward unity only at higher photon energies. A secondary peak near 20–22 eV mirrors the corresponding feature in $\varepsilon_2(\omega)$ and is again attributed to cation semi-core excitations.

The extinction coefficient $K(\omega) = \mathrm{Im}[\sqrt{\varepsilon(\omega)}]$ quantifies the attenuation of the wave amplitude per unit optical path and is directly related to the absorption coefficient via $\alpha = {}^{2\omega K}/_{C}$. In the sub-gap region, $K(\omega)$ is identically zero for all three materials, confirming transparency below the respective band edges. The extinction spectrum rises sharply at threshold and develops two clearly resolved absorption bands separated by a plateau region of comparatively low extinction.

The first band, spanning roughly 4–14 eV depending on the compound, is dominated by halide p → metal d transitions. $KSrBr_3$ peaks earliest ~5 eV and most strongly ≈ 1.35 within this band, followed by $KSrCl_3$ K ≈ 1.28 near 6.5 eV. $KSrF_3$, with its wider gap, exhibits a lower and broader first-band envelope. The second band near 20–22 eV is associated with cation semi-core transitions and shows comparable peak heights ~ 0.9–1.3 across the series, with $KSrF_3$ displaying the largest extinction in this region, reaching approximately 1.33 near 22 eV. This inversion relative to the first band reflects the increasing oscillator strength of the F-associated cation environment at high excitation energies.

The absorption coefficient α in Fig 7(c) provides the most direct measure of how effective each compound attenuates light as a function of photon energy. The computed spectra show that absorption is negligible for photon energies below the respective corrected band gaps, consistent with the wide-gap semiconductor character of the $KSrX_3$ series. Absorption rises steeply at threshold, and each compound exhibits two principal absorption bands whose origins mirror those identified in $\varepsilon_2(\omega)$ and $K(\omega)$.

The first absorption band, which peaks in the 5–14 eV window, attains maximum values for $KSrBr_3$, $KSrCl_3$, and $KSrF_3$ of roughly 75, 80, and 85, respectively. Although the onset of this band shifts to lower energies with increasing halide polarisability (F → Cl → Br), the absolute peak absorption at these near-ultraviolet to vacuum-ultraviolet energies is comparable across the series, indicating that the joint density of optical states is similarly large in all three compounds once the gap is bridged.

A substantially more intense second absorption band emerges near 20–22 eV, reaching peak values of approximately 185 ($KSrCl_3$), 190 ($KSrBr_3$), and 235 ($KSrF_3$). The existence of strong absorption in the extreme ultraviolet region indicates that these halide perovskites are potential candidates for UV-related applications.

E. Thermodynamic properties

The thermodynamic stability and thermal response of a crystalline solid are among the most practically significant quantities accessible from first-principles simulations.

Knowledge of the temperature dependence of enthalpy, Gibbs free energy, entropy, and heat capacity is necessary for determining the phase stability under operating conditions and for relating a material against standard structural analogues [33-34]. In the present work, the quasi-harmonic Debye approximation, as implemented within the GIBBS2 formalism [33], was employed to evaluate these thermodynamic functions over the temperature range 0–800 K at zero pressure for the three compounds $KSrF_3$, $KSrCl_3$, and $KSrBr_3$.

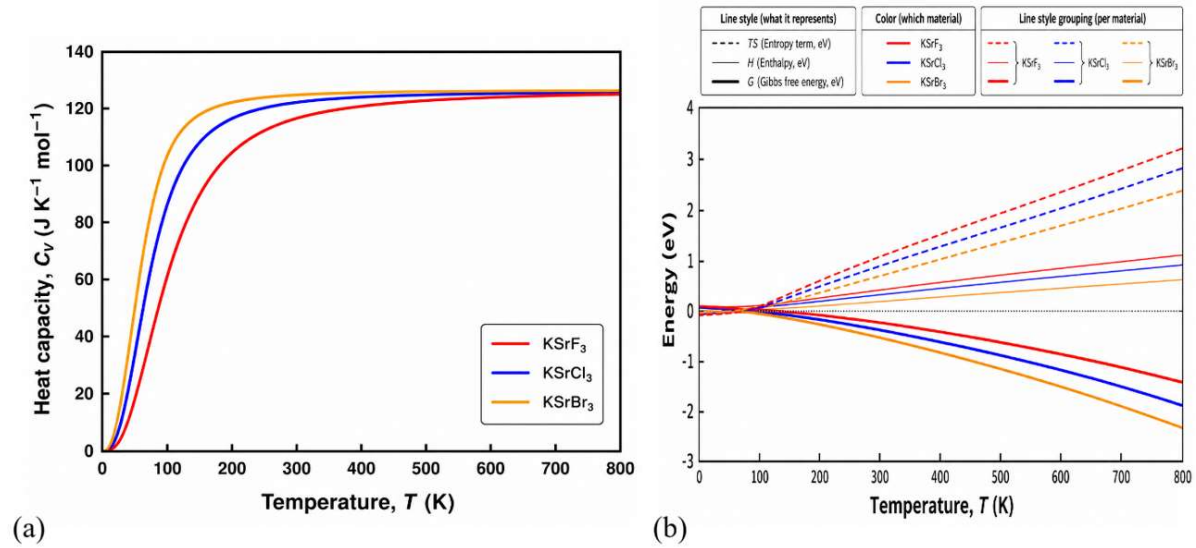

Fig. 8. (a) Heat capacity C_v in (J/K/(N mol)) (b) Enthalpy (dashed line), TS (thin line), and Gibbs free energy (thick line) all in eV of compounds $KSrF_3$ (red), $KSrCl_3$ (blue), and $KSrBr_3$ (yellow) against Temperature (K).

The temperature dependences of the vibrational contributions to enthalpy (*H*), Gibbs free energy (*G*), and entropy term (TS) in Fig. 8(b) are fully consistent with the expectations of lattice dynamics for wide-gap ionic solids [35]. At 0 K, all three quantities are ~ zero, conforming to the third law of thermodynamics, and they increase monotonically with temperature thereafter. This behavior is usually observed in perovskite-type compounds [36].

Enthalpy increases linearly with temperatures beyond roughly 200 K, indicative of the classical equipartition regime in which most phonon branches are thermally active. At 800 K, the computed enthalpies reach approximately 1.0 eV ($KSrF_3$), 0.95 eV ($KSrCl_3$), and 0.93 eV ($KSrBr_3$).

The Gibbs free energy, which combines enthalpy with the entropic contribution through the relation $G = H - TS$, becomes increasingly negative with rising temperature. At 800 K, the free energies are approximately −1.3 eV ($KSrF_3$), −1.5 eV ($KSrCl_3$), and −2.0 eV ($KSrBr_3$). The greater negative deviation observed for $KSrBr_3$ is consistent with its softer lattice and higher vibrational entropy: the lower-frequency phonon spectrum of the bromide compound leads to a larger entropic driving force at elevated temperatures [37]. Similar trends have been reported for the isostructural series $RbSrX_3$ (X = F, Cl, Br, I) studied by Fatima *et al.,* [36], where progressively heavier halides were found to exhibit larger entropic contributions to the free energy.

The entropy term TS, shown with a broken curve in Fig. 8(b), increases steeply and near-linearly above approximately 150 K, reaching values close to 2.2 eV ($KSrF_3$), 2.6 eV ($KSrCl_3$), and 3.3 eV ($KSrBr_3$) at 800 K. The ordering $TS(KSrBr_3) > TS(KSrCl_3) > TS(KSrF_3)$ reflects that compounds with larger, more polarizable anions have lower Debye temperatures and therefore a denser distribution of thermally accessible phonon states at any given temperature [33, 38].

The heat capacity at constant volume, $C_v(T)$, calculated using the second temperature derivative of the Helmholtz free energy, is shown in Fig. 8(a). At very low temperatures (T = 0 K), C_v follows the T^3 power law predicted by the Debye model for acoustic phonon contributions in three dimensions [38-39]. According to the curve, all three compounds exhibit a near-cubic rise from zero at 0 K, transitioning to a more gradual increase above approximately 80–150 K.

A notable distinction across the series is the temperature at which C_v begins its rapid rise. $KSrBr_3$ reaches appreciable values at the lowest temperatures, with a steep onset commencing near 20–30 K, followed by $KSrCl_3$ (onset near 40–50 K) and then $KSrF_3$ (onset near 60–80 K). This ordering directly reflects the Debye temperature sequence: $KSrF_3$ has the stiffest lattice and the highest Debye temperature, meaning more thermal energy is required to activate its phonon modes relative to the chloride and bromide compounds. References [35] and [37] documented the same trend in analogous K-based chloride perovskites, and in the Sn-based halide perovskites $ASnCl_3$ (A = Na, K), respectively.

At intermediate temperatures (200–500 K), the C_v curves for all three compounds converge toward a common asymptote. Beyond approximately 500 K, the heat capacities saturate and approach the classical Dulong–Petit limit of $C_v \sim 3nN_Ak_B$, where n is the number of atoms per formula unit and $N_Ak_B = R$. For a five-atom unit cell this limit is $5 \times 3R \approx 124.7$ J K^{-1} mol^{-1}, which is in excellent agreement with the computed saturation value of approximately 124–125 J K^{-1} mol^{-1} observed for all three compounds [40-41]. The attainment of the Dulong–Petit limit confirms the completeness of the phonon mode spectrum included in the quasi-harmonic Debye calculation and serves as an important internal validation of the thermodynamic model.

IV. Conclusion

DFT calculations using Quantum ESPRESSO were systematically employed to analyze the structural, electronic, phonon, mechanical, optical, and thermodynamic properties of Sr-based halide perovskites $KSrX_3$ (X = F, Cl, and Br). Structural optimization and tolerance factors confirm that all three compounds possess a stable cubic perovskite structure and are thermodynamically feasible, as evidenced by negative formation energies. The electronic structure computed using GGA-PBE reveals the insulating behavior, with an indirect band gap of 3.75 and 4.45 eV for $KSrBr_3$ and $KSrCl_3$, respectively, and a direct band gap of 5.52 eV for $KSrF_3$. The systematic decrease in band gap from F → Cl → Br demonstrates halide-dependent band gap tunability, suggesting that external stimuli such as pressure or epitaxial strain could be employed to further engineer electronic structure for target applications. Elastic properties for the three materials indicate mechanical stability. It was found that all the compounds are elastically anisotropic and ductile in nature. High absorption in the UV range, suggesting KSrX3 compounds are promising candidates for UV optoelectronic devices. Experimental synthesis and high-temperature characterization are needed to verify these predictions.

References

[1] U.-G. Jong, C.-J. Yu, Y.-H. Kye, Y.-G. Choe, W. Hao, and S. Li, "First-principles study on structural, electronic, and optical properties of inorganic Ge-based halide perovskites," Inorg. Chem., vol. 58, no. 7, pp. 4134-4140, 2019, doi: 10.1021/acs.inorgchem.8b03095.

[2] J.-H. Lee, Z. Deng, N. C. Bristowe, P. D. Bristowe, and A. K. Cheetham, "The competition between mechanical stability and charge carrier mobility in MA-based hybrid perovskites: insight from DFT," J. Mater. Chem. C, vol. 6, pp. 12252-12259, 2018, doi: 10.1039/C8TC04750B.

[3] A. Zia, G. Murtaza, K. Ismail, R. M. A. Khalil, and M. I. Hussain, "Ab-initio calculations of the structural, electronic and optical response of $KXCl_3$ (X = Be, Ca and Sr) for optoelectronic applications," Comput. Condens. Matter, vol. 33, p. e00737, 2022, doi: 10.1016/j.cocom.2022.e00737.

[4] J. Khan, W. Udin, S. U. Rahman, K. S. Almaary, Y. A. Bin Jardan, A. A. M. Al-Harethi, T. A. Shah, and R. Ajaj, "Enhancing the optoelectronic and mechanical response of MgXCl3 (X = Rb, Ca) for advance energy conversion applications," Sci. Rep., vol. 15, no. 1, p. 29509, 2025, doi: 10.1038/s41598-025-97019-x.

[5] R. A. Solomon and O. M. Kayode, "Emerging strategies in phase-tuned perovskite materials for efficient hydrogen evolution: a machine learning perspective," FUDMA J. Sci., vol. 9, no. 8, pp. 93-98, 2025, doi: 10.33003/fjs-2025-0908-3894.

[6] A. M. Nura, S. R. Haladu, A. S. Gidado, L. Abubakar, and R. S. Abraham, "Determination of structural, electronic, and elastic properties of $SnTiO_3$ using density functional theory," PHYSICSAccess, vol. 4, no. 2, pp. 17-23, 2024, doi: 10.47514/phyaccess.2024.4.2.002.

[7] B. Fadila, M. Ameri, D. Bensaid, M. Noureddine, I. Ameri, S. Mesbah, and Y. Al-Douri, "Structural, magnetic, electronic and mechanical properties of full-Heusler alloys Co_2YAl (Y = Fe, Ti): First principles calculations with different exchange-correlation potentials," J. Magn. Magn. Mater., vol. 448, pp. 208-220, 2018, doi: 10.1016/j.jmmm.2017.06.048.

[8] M. Ameri, S. Amel, B. Abidri, I. Ameri, Y. Al-Douri, B. Bouhafs, D. Varshney, A. Aze-Eddine, and L. Nadia, "Structural, elastic, electronic and thermodynamic properties of uranium filled skutterudites UFe_4P1_2: First principle method," Mater. Sci. Semicond. Process., vol. 27, pp. 368-379, 2014, doi: 10.1016/j.mssp.2014.06.054.

[9] B. T. Huy and J. H. Shin, "Perovskite materials for sensing applications: recent advances and challenges," Microchem. J., vol. 191, p. 108924, 2023, doi: 10.1016/j.microc.2023.108924.

[10] S. Soltani, M. Hjiri, N. I. A. Ahmed, A. Jbeli, A. M. Aldukhayel, and N. A. Althumairi, "Metal halide perovskites for energy applications: recent advances, challenges, and future perspectives," RSC Adv., vol. 15, no. 27, pp. 21811-21837, 2025, doi: 10.1039/d5ra02730f.

[11] S.-Y. Kim, Y. Yun, S. Shin, J. H. Lee, Y.-W. Heo, and S. Lee, "Wide range tuning of band gap energy of $A_3B_2X_9$ perovskite-like halides," Scr. Mater., vol. 166, pp. 107-111, 2019, doi: 10.1016/j.scriptamat.2019.03.009.

[12] G. Murugadoss, S. Tanaka, G. Mizuta, S. Kanaya, H. Nishino, T. Umeyama, H. Imahori, and S. Ito, "Light stability tests of methylammonium and formamidinium Pb-halide perovskites for solar cell applications," *Jpn. J. Appl. Phys.*, vol. 54, no. 8S1, Art. no. 08KF08, Jul. 2015, doi: 10.7567/JJAP.54.08KF08.

[13] J. I. Gómez-Peralta and X. Bokhimi, "Ternary halide perovskites for possible optoelectronic applications revealed by artificial intelligence and DFT calculations," Mater. Chem. Phys., vol. 267, p. 124710, 2021, doi: 10.1016/j.matchemphys.2021.124710.

[14] M. Y. Khan, M. A. Jehangir, I. E. Lee, Q. Wali, T. Usman, X. Li, and A. Al Souwaileh, "First-principles study of $XSrBr_3$ (X = Li, K, Ag) halide perovskites for solar-blind photodetector applications," Chem. Phys. Impact, vol. 11, p. 100933, 2025, doi: 10.1016/j.chphi.2025.100933.

[15] A. A. Mousa, M. S. Abu-Jafar, D. Dahliah, R. M. Shaltaf, and J. M. Khalifeh, "Investigation of the perovskite $KSrX_3$ (X = Cl and F) compounds, examining the optical, elastic, electronic and structural properties: FP-LAPW study," J. Electron. Mater., vol. 47, no. 1, pp. 641-650, 2018, doi: 10.1007/s11664-017-5817-x.

[16] P. Giannozzi et al., "QUANTUM ESPRESSO: a modular and open-source software project for quantum simulations of materials," J. Phys.: Condens. Matter, vol. 21, no. 39, p. 395502, 2009, doi: 10.1088/0953-8984/21/39/395502.

[17] W. Kohn and L. J. Sham, "Self-consistent equations including exchange and correlation effects," Phys. Rev., vol. 140, no. 4A, pp. A1133-A1138, 1965, doi: 10.1103/PhysRev.140.A1133.

[18] N. Ahmed, J. Nisar, R. Kouser, A. G. Nabi, S. Mukhtar, Y. Saeed, and M. H. Nasim, "Study of electronic, magnetic and optical properties of KMS2 (M = Nd, Ho, Er and Lu): first principle calculations," Mater. Res. Express, vol. 4, no. 6, p. 065903, 2017, doi: 10.1088/2053-1591/aa75fc.

[19] S. Haid, W. Benstaali, A. Abbad, B. Bouadjemi, S. Bentata, and Z. Aziz, "Thermoelectric, structural, optoelectronic and magnetic properties of double perovskite Sr_2CrTaO_6: first principle study," Mater. Sci. Eng. B, vol. 245, pp. 68-74, 2019, doi: 10.1016/j.mseb.2019.05.013.

[20] A. S. Gidado, R. A. Solomon, L. Abubakar, F. Ahmed, and S. R. Haladu, "First principle investigations of structural, electronic and thermal properties of pristine, metal and non-metal doped silicene for thermoelectric applications," PHYSICSAccess, vol. 4, no. 2, pp. 85-94, 2024, doi: 10.47514/phyaccess.2024.4.2.010.

[21] M. Born and K. Huang, Dynamical Theory of Crystal Lattices, 1st ed. Oxford, U.K.: Clarendon Press, 1954.

[22] Z. Jellil, A. Idrissi el Oudrhiri, H. Jebari, A. Soussi, M. Eddekkar, I. Ez-Zejjari, and H. Ez-Zahraouy, "Band gap shifting of halide perovskite KSrCl3 from ultra-violet to visible region under pressure for photovoltaic applications," Micro Nanostruct., vol. 193, p. 207911, 2024, doi: 10.1016/j.micrna.2024.207911.

[23] S. K. Mitro, M. Saiduzzaman, A. Biswas, A. Sultana, and K. M. Hossain, "Electronic phase transition and enhanced optoelectronic performance of lead-free halide perovskites $AGeI_3$ (A = Rb, K) under pressure," Mater. Today Commun., vol. 31, p. 103532, 2022, doi: 10.1016/j.mtcomm.2022.103532.

[24] D. Abdullah and D. C. Gupta, "Exploring the structural, mechanical, electronic, optical, and thermoelectric properties of cesium-based double perovskite Cs_2GeSnX_6 (X = Cl, Br, I) compounds: a DFT study," Mater. Sci. Semicond. Process., vol. 167, p. 107813, 2023, doi: 10.1016/j.mssp.2023.107813.

[25] Z. Li, M. Yang, J.-S. Park, S.-H. Wei, J. J. Berry, and K. Zhu, "Stabilizing perovskite structures by tuning tolerance factor: formation of formamidinium and cesium lead iodide solid-state alloys," Chem. Mater., vol. 28, no. 1, pp. 284-292, 2016, doi: 10.1021/acs.chemmater.5b04107.

[26] M. E. Sarhani, T. Dahame, M. L. Belkhir, B. Bentria, and A. Begagra, "Ab-initio study of electronic, mechanical, optical and thermoelectric properties of $KGeCl_3$ for photovoltaic application," Heliyon, vol. 9, no. 9, p. e19808, 2023, doi: 10.1016/j.heliyon.2023.e19808.

[27] Y. Wen, L. Wang, H. Liu, and L. Song, "Ab initio study of the elastic and mechanical properties of B19 TiAl," Crystals, vol. 7, no. 2, p. 39, 2017, doi: 10.3390/cryst7020039.

[28] D. Connétable and O. Thomas, "First-principles study of the structural, electronic, vibrational, and elastic properties of orthorhombic NiSi," Phys. Rev. B, vol. 79, no. 9, p. 094101, 2009, doi: 10.1103/PhysRevB.79.094101.

[29] G. Surucu, A. Gencer, A. Candan, H. H. Gullu, and M. Isik, "$CaXH_3$ (X = Mn, Fe, Co) perovskite-type hydrides for hydrogen storage applications," Int. J. Energy Res., vol. 44, no. 3, pp. 2345-2354, 2020, doi: 10.1002/er.5062.

[30] V. Brazhkin, A. Lyapin, S. Popova, A. Antonov, A. Kluvev and A. Naletov, "Mechanical properties of the superhard polymeric and disordered phases prepared from C60, C70 and C_2N under high pressure," Japan Society of High Pressure Science and Technology, vol. 7, pp 989-991, 1998, doi: 10.4131/jshpreview.7.989.

[31] S. Ranganathan and O. Martin, "Universal elastic anisotropy index," Physical Review Letters, vol. 10, no. 5, 2008, doi: 10.1103/PhysRevLett.101.055504.

[32] G. Murtaza and I. Ahmad, "First principle study of the structural and optoelectronic properties of cubic perovskites $CsPbM_3$ (M = Cl, Br, I)," Phys. B Condens. Matter, vol. 406, no. 17, pp. 3222-3229, 2011, doi: 10.1016/j.physb.2011.05.028.

[33] M. A. Blanco, E. Francisco, and V. Luaña, "GIBBS: isothermal-isobaric thermodynamics of solids from energy curves using a quasi-harmonic Debye model,"

Comput. Phys. Commun., vol. 158, no. 1, pp. 57-72, 2004, doi: 10.1016/j.comphy.2003.12.001.

[34] A. Bouhmouche, S. Tariq, A. Jabar, R. Moubah, H. Lassri, and M. Abid, "Electronic and thermodynamic properties of $CsPbI_3$ halide perovskites: Ab-initio investigation," Mater. Today Proc., 2023, doi: 10.1016/j.matpr.2023.10.102.

[35] A. Bedjaoui, D. Allali, M. Radjai, A. Bouhemadou, S. S. Essaoud, S. Bin-Omran, R. Khenata, and Y. Al-Douri, "Ab initio predictions of pressure-dependent structural, elastic, and thermodynamic properties of $GaMF_3$ (M = Ca, and Sr) halide perovskites," Solid State Commun., vol. 387, p. 115532, 2024, doi: 10.1016/j.ssc.2024.115532.

[36] T. Fatima, A. W. Anwar, S. Nabi, A. Ali, M. B. Shakir, S. Ali, U. Javed, S. Shaheen, and S. Ahmad, "DFT-based study of structural, mechanical, electronic, thermodynamic, and optical properties of wide band gap $RbSrX_3$ (X = F, Cl, Br, I) halides: promising materials for optoelectronic applications," J. Phys. Chem. Solids, vol. 208, p. 113157, 2026, doi: 10.1016/j.jpcs.2025.113157.

[37] N. Iram, R. Sharma, J. Ahmad, A. Kumar, A. Kumar, F. N. Almutairi, and H. A. Alturaifi, "A DFT manifestation of the physical, thermodynamic and thermoelectric properties in Sn-based halide perovskites $ASnCl_3$ (A = Na, K)," Inorg. Chem. Commun., vol. 172, p. 113573, 2025, doi: 10.1016/j.inoche.2024.113573.

[38] S. S. Essaoud, A. Bouhemadou, M. E. Ketfi, M. Radjai, and D. Allali, "DFT + U based characterization of structural, magnetic, dynamic, elastic and thermodynamic properties of KXF_3 (X = Fe or Co) halide perovskites compounds," Chem. Phys. Lett., vol. 850, p. 141455, 2024, doi: 10.1016/j.cplett.2024.141455.

[39] M. Kmichou and R. Masrour, "First principles calculations of structural, phonon, mechanical, optoelectronic, photovoltaic, thermoelectric and thermodynamic properties of inorganic novel cubic halide perovskites Ca_3AsX_3 (X = Br, I): a DFT study," Adv. Theory Simul., vol. 8, no. 8, 2025, doi: 10.1002/adts.202500087.

[40] D. Abdullah and D. C. Gupta, "DFT simulations of the elastic, optoelectronic, and thermoelectric attributes of $AOsCl_3$ (A = K, Rb), a robust and environmentally friendly perovskites for green energy implications," Sci. Rep., vol. 14, no. 1, p. 26168, 2024, doi: 10.1038/s41598-024-73412-w.

[41] Md. Tarekuzzaman, N. Shahadath, M. Montasir, O. Alsalmi, M. H. Mia, H. Al-Dmour, Md. Rasheduzzaman, and Md. Z. Hasan, "DFT analysis of the physical properties of direct band gap semiconducting double perovskites A_2BIrCl_6 (A = Cs, Rb; B = Na, K) for solar cells and optoelectronic applications," RSC Adv., vol. 15, no. 17, pp. 13643-13661, 2025, doi: 10.1039/D5RA01748C.